



HAL
open science

High-reflectivity Si_3N_4 photonic-crystal membranes for optomechanics

X Chen, C Chardin, K Makles, C Caër, S Chua, R Braive, I Robert-Philip, T Briant, P.-F Cohadon, A Heidmann, et al.

► **To cite this version:**

X Chen, C Chardin, K Makles, C Caër, S Chua, et al.. High-reflectivity Si_3N_4 photonic-crystal membranes for optomechanics. 2016. hal-01291712v1

HAL Id: hal-01291712

<https://hal.science/hal-01291712v1>

Preprint submitted on 23 Mar 2016 (v1), last revised 1 Jun 2016 (v2)

HAL is a multi-disciplinary open access archive for the deposit and dissemination of scientific research documents, whether they are published or not. The documents may come from teaching and research institutions in France or abroad, or from public or private research centers.

L'archive ouverte pluridisciplinaire **HAL**, est destinée au dépôt et à la diffusion de documents scientifiques de niveau recherche, publiés ou non, émanant des établissements d'enseignement et de recherche français ou étrangers, des laboratoires publics ou privés.

Public Domain

High-reflectivity Si_3N_4 photonic-crystal membranes for optomechanics

X. Chen,¹ C. Chardin,¹ K. Makles,¹ C. Caër,^{1,*} S. Chua,¹ R. Braive,^{2,3} I. Robert-Philip,²
T. Briant,¹ P.-F. Cohadon,¹ A. Heidmann,¹ T. Jacqmin,¹ and S. Deléglise¹

¹*Laboratoire Kastler Brossel, UPMC-Sorbonne Universités, CNRS, ENS-PSL Research
University, Collège de France, 4 place Jussieu, Case 74, F75252 Paris Cedex 05, France*

²*Laboratoire de Photonique et de Nanostructures LPN-CNRS/CNRS, Route de Nozay, 91460 Marcoussis, France*

³*Université Paris Diderot, Sorbonne Paris Cité, 75207 Paris Cedex 13, France*

(Dated: March 23, 2016)

ABSTRACT

Nanomechanical resonators strongly coupled to the electromagnetic field are a promising resource for quantum-limited mass and force sensors, and as transducers for coupling otherwise incompatible quantum systems such as microwave and optical photons. In particular, suspended nanomembranes obtained by chemical release of a high-tensile stress layer are an advantageous platform for such transducers, combining an extremely high mechanical quality factor and a low mass. We demonstrate the successful implementation of a photonic-crystal reflector on a high-tensile stress Si_3N_4 nanomembrane, enabling its direct coupling to a high-finesse optical cavity. This approach is particularly well suited for hybrid opto-electro-mechanical transducers, where the membrane motion is simultaneously coupled to an optical and a microwave cavity. We provide an illustration of the physical process underlying the high reflectivity by measuring the photonic crystal band diagram. Moreover, we introduce a clear theoretical description of the membrane scattering properties in the presence of optical losses. By embedding the photonic-crystal membrane inside a high-finesse cavity, we fully characterize its optical properties. The spectrally resolved measurements demonstrate the wide tunability of the membrane's reflectivity, from nearly 0 to $99.79 \pm 0.02\%$, and show that the material absorption is not the main source of optical losses.

INTRODUCTION

The radiation-pressure interaction between light and moving mechanical resonators has been the subject of an intense growing research program over the last decade. Several experiments have reached a regime where a quantum mechanical description of both mechanical and optical degrees of freedom is required [1–3]. This research program is currently broadly driven by fundamental objectives such as understanding the consequences of quantum mechanics on continuous measurements [4] or study-

ing quantum superposition and decoherence of macroscopic objects [5]. Further, optomechanical systems are candidates to couple otherwise incompatible quantum systems, such as recently demonstrated with superconducting qubits [6], quantum dots [7], spins [8, 9] or cold atoms [10]. In addition, they constitute a promising resource for classical and quantum transducers, as they can be used to up-convert microwave signals onto an optical carrier for subsequent detection or transmission into optical fibers [11, 12].

Suspended membranes made from thin layers of highly stressed materials are an advantageous platform for the development of optomechanical transducers as they combine an excellent mechanical Q-factor [13], a low mass and a relatively low mechanical resonance frequency that results in large quantum zero-point motion. Moreover, they are readily integrable with electromechanical systems by using them as the moving electrode of a parallel plate capacitor [14], or by exploiting dielectric gradient forces [15, 16] to couple them to a nearby planar capacitor. On the other hand, a high-finesse optical cavity, operating in the resolved sideband regime [17], is required to efficiently couple the membrane motion to the optical field. Given the very low thickness of the vibrating membrane, alternative strategies to the usual multilayer dielectric high-reflection coatings have to be used. One approach is to exploit the dispersive coupling between the membrane motion and the mode of a high-finesse cavity inside which it is placed [18]. This technique does allow the reaching of high optical finesse, however it requires a complex optical alignment and for low-reflectivity membranes, the optomechanical coupling is reduced compared to a cavity in the moving-mirror configuration. Another approach is to use photonic-crystal techniques to increase the membrane reflectivity without affecting its motional mass [16, 19].

Here, we report on the implementation and full optical characterization of a 2D photonic crystal membrane (PhC) directly etched on a high tensile stress 200 nm-thick Si_3N_4 nanomembrane. To our knowledge, this is the first successful implementation of this technique on a high-tensile stress nanomembrane. By measuring for the first time the band diagram of the guided resonances in the 2D photonic crystal with an angle resolved spectrometer, we shed new light on the physics of these structures.

Moreover, we measure a PhC reflectivity of $99.79 \pm 0.02\%$ at 1079.1 nm and show that it is not yet limited by material absorption. Finally, we introduce a clear theoretical description of the scattering properties of the PhC in the presence of optical losses. Our experiments demonstrate the wide range of validity of the Rigorous Coupled Wave Analysis (RCWA) and the corresponding tunability of the membrane reflectivity versus optical wavelength, which is beneficial for optomechanical experiments where the tunnelling rate through the membrane needs to be matched with the mechanical resonance frequency [20].

METHODS

A. Membrane and photonic crystal fabrication

The commercial membranes [21] are made of a 200 nm stoichiometric Si_3N_4 film deposited on a Si substrate and released over a 1 mm \times 1 mm square by chemical etching of the substrate (see Fig. 1a). High tensile stress in the film ensures mechanical modes with quality factors as high as 10^8 at low temperature [22] and ultra-low mass [13]. The photonic crystal is realized in the centre of the membrane. It is obtained by electron-beam lithography on a layer of 200 nm of Poly(methyl methacrylate) (PMMA) resist, followed by reactive ion etching with a plasma of CHF_3 and SF_6 . The PMMA is then stripped off with an oxygen plasma. The photonic crystal consists of a 270- μm diameter disk patterned with a square lattice of circular holes (see Fig. 1). The lattice parameter is $\Lambda = 830$ nm, and the design value for the hole radius is 293 nm.

B. PhC characterization

Band diagram measurement

We implemented the white-light illumination and imaging setup shown in Fig. 2(a) to measure the PhC band diagram. A halogen white lamp is combined with a set of 3 lenses (L_1, L_2, L_3) and two diaphragms (D_1, D_2) to realize a Köhler illumination configuration. A field diaphragm (D_1) conjugated to the PhC restricts the illumination to the PhC area thus reducing the impact of light scattered on optical elements and mounts. The aperture diaphragm (D_2) is used to select the incident beam angles at the PhC position. It is centred on the optical axis and its aperture width is chosen to reject high angle-of-incidence components that are irrelevant for this experiment. A magnified image of the PhC is obtained with a microscope objective (L_4) and a lens (L_5). At the image plane sits a field diaphragm (D_3), conjugated

to diaphragm (D_1), providing additional filtering of unwanted scattered light. A fiber tip is positioned in the focal plane of lens (L_6), that is in the Fourier plane of this imaging system. The light collected by the fiber is guided to a near-infrared spectrometer. By scanning the fiber in the transverse (x, y) plane the transmission spectrum can be measured at different angles. Moreover, a polarizer (Pol) is introduced between (L_1) and (L_2) for polarization selection.

PhC reflection, transmission and losses measurements

We implemented a single-ended cavity with the PhC as the end-mirror (Fig. 2b) to characterize its reflectivity, transmission and losses. The input mirror of the cavity is a 10 mm radius-of-curvature mirror and the cavity length is 4.1 mm. This ensures a waist size $w_0 = 41 \mu\text{m}$ located on the PhC, smaller than the lateral extent of the photonic crystal, and an angular dispersion $\Delta\theta = \arctan(\lambda/\pi w_0) = 8.3 \times 10^{-3}$ rad that has a negligible influence on the optical properties of the PhC. A motorized Littman-Metcalf stabilized diode laser system from Sacher GMBH (Lion TEC-520) is used to probe the cavity. The cavity transmission is monitored with an avalanche photodiode (Thorlabs APD110C), and recorded continuously while the laser frequency is scanned over 4.8 nm. Simultaneously, the fringes of an imbalanced fiber interferometer are counted by a digital system (based on an Arduino micro-controller [23]) to measure the laser frequency in real time. The free spectral range, bandwidth and visibility of each peak are extracted from Lorentzian fits.

Description and characterization of the PhC losses

In the following we provide a complete theoretical description of the PhC optical properties in the presence of losses. The membrane can be described by its scattering matrix, transforming the fields $a_{\text{in},l}, a_{\text{in},r}$ incoming from left and right into outgoing fields $a_{\text{out},l}, a_{\text{out},r}$ (see Fig. 2b):

$$\begin{pmatrix} a_{\text{out},l} \\ a_{\text{out},r} \end{pmatrix} = S \begin{pmatrix} a_{\text{in},l} \\ a_{\text{in},r} \end{pmatrix}, \quad (1)$$

$$\text{with } S = \begin{pmatrix} r & \bar{t} \\ t & \bar{r} \end{pmatrix} = \begin{pmatrix} r & t \\ t & r \end{pmatrix}, \quad (2)$$

where the symmetry of the membrane with respect to the xOy plane is used to assume that the direct (r, t) and reciprocal (\bar{r}, \bar{t}) complex reflection and transmission amplitudes are equal. The previous assumption allows S to be diagonalized

$$S = V \begin{pmatrix} r+t & 0 \\ 0 & r-t \end{pmatrix} V^{-1},$$

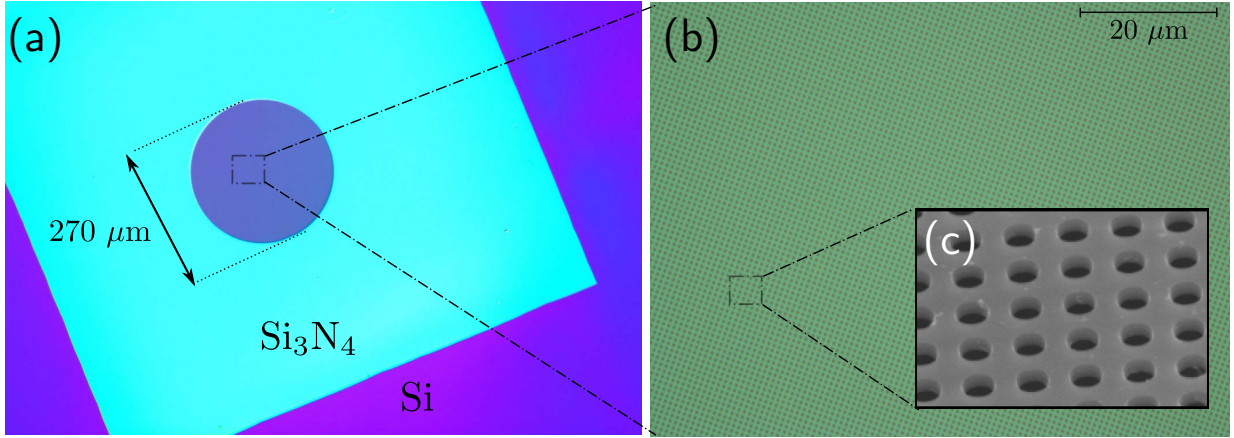


FIG. 1. (a) Optical image of the PhC made of a high-stress Si₃N₄ membrane suspended on a Si frame. The disk in the centre is the photonic crystal. (b) Optical microscope image of the PhC. (c) Scanning electron micrograph of the PhC.

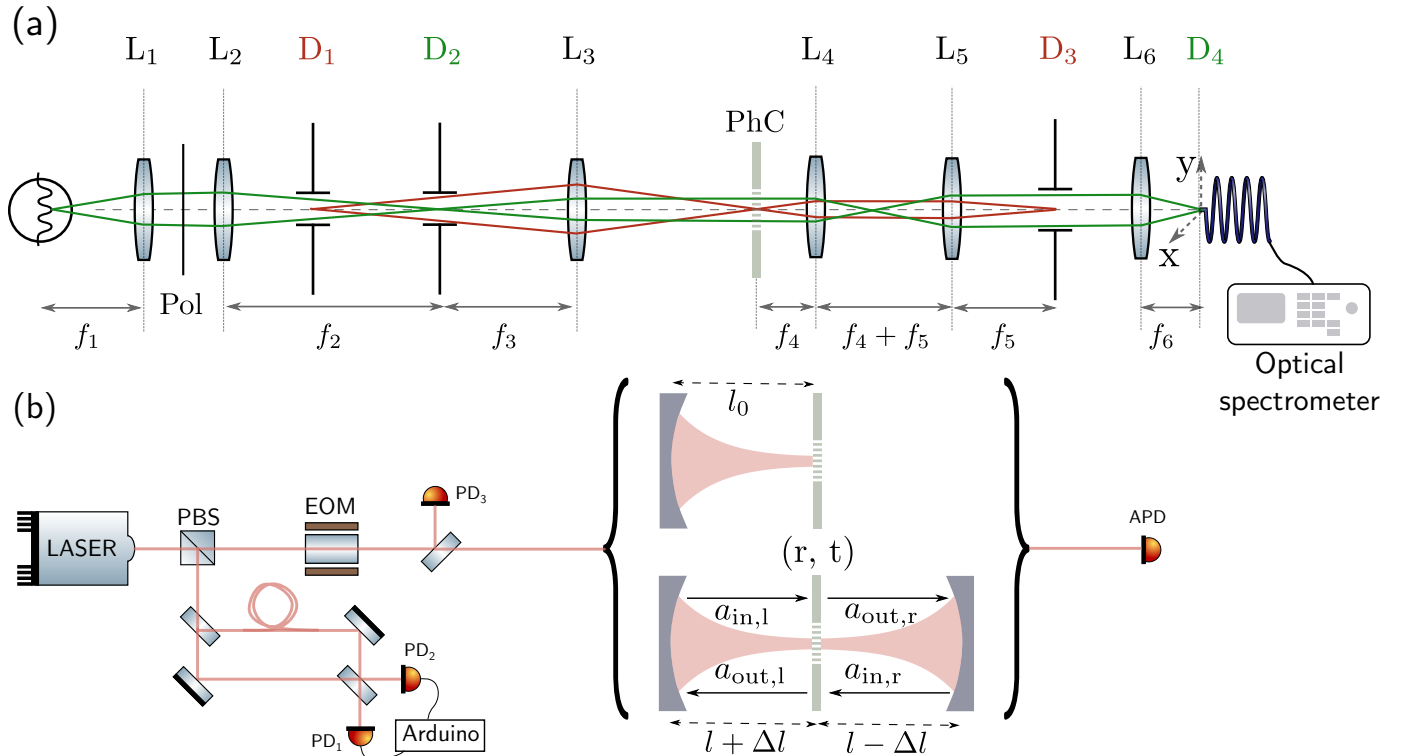


FIG. 2. (a) Setup used to record the PhC band structure. The light source is a Thorlabs tungsten halogen white lamp (SLS201). The illumination system is made of three lenses (L_1 , L_2 , L_3) and two diaphragms (D_1 , D_2). The imaging system is made of one microscope objective (L_4), two lenses (L_5 , L_6) and two diaphragms (D_3 , D_4), (D_4) being the fiber tip which can be scanned along the x and y directions. (Pol) is a linear polarizer and (PhC) is the photonic-crystal sample. The green rays are the Fourier image rays whereas the red rays are the real image rays. (b) Fabry-Perot cavity setups used to measure the membrane reflectivity and losses: the transmission of the cavity is measured by an avalanche photodiode (APD), and normalized by the incident signal from the photodiode (PD₃). For the single-ended cavity measurement (top cavity and Fig. 4), the laser diode is continuously scanned while an imbalanced interferometer is used to monitor its wavelength (PD₁, PD₂), and 50-MHz sidebands are generated by an electrooptic modulator (EOM). For the membrane-in-the-middle measurement (bottom cavity and Fig. 5), the laser wavelength and membrane positions are scanned by piezoelectric actuators on the grating of the Littmann-Metcalf laser system and on the membrane mount respectively. (PBS): Polarizing Beam Splitter.

with the change of basis

$$V = \frac{1}{\sqrt{2}} \begin{pmatrix} 1 & 1 \\ 1 & -1 \end{pmatrix}$$

For a lossless membrane, S is unitary ($|r+t| = |r-t| = 1$), such that within a global phase factor, it is entirely determined by a single real parameter, for instance the intensity transmission $T = |t|^2$. However, in the presence of losses, the scattered fields have a total intensity smaller than the input fields and both eigenvalues obey

$$|r+t| \leq 1 \quad (3)$$

$$|r-t| \leq 1. \quad (4)$$

Three real parameters (plus a global phase term) are required to fully describe S : in addition to the intensity transmission T , we introduce the optical losses

$$L_{\pm} = 1 - |r \pm t|^2 \quad (5)$$

associated to the symmetric and antisymmetric combinations of left and right incoming fields $\begin{pmatrix} a_{\text{in},l} \\ a_{\text{in},r} \end{pmatrix} \propto \frac{1}{\sqrt{2}} \begin{pmatrix} 1 \\ \pm 1 \end{pmatrix}$. To obtain a measurement of L_{\pm} , the membrane can be positioned in the centre of a high-finesse cavity. This setup, initially proposed in the group of J. Harris [18], consists of two single-ended cavities coupled via the transmission of the membrane. If the input and output mirrors have the same amplitude reflectivity r' and if both sub-cavities have the same length l , one gets in the absence of fields incident from outside the cavity (see Fig. 2b):

$$a_{\text{in},l} = tr'e^{-2ikl}a_{\text{in},r} + rr'e^{-2ikl}a_{\text{in},l} \quad (6)$$

$$a_{\text{in},r} = tr'e^{-2ikl}a_{\text{in},l} + rr'e^{-2ikl}a_{\text{in},r}, \quad (7)$$

where $k = \tilde{\omega}/c$ is the wave-number of the propagating field. The eigenmodes of the total optical cavity correspond to non-trivial solutions of this system for complex angular frequencies $\tilde{\omega}$. By taking the sum and difference of the previous equations, we obtain

$$a_{\text{in},l} + a_{\text{in},r} = (r+t)r'e^{-2ikl} [a_{\text{in},l} + a_{\text{in},r}] \quad (8)$$

$$a_{\text{in},l} - a_{\text{in},r} = (r-t)r'e^{-2ikl} [a_{\text{in},l} - a_{\text{in},r}]. \quad (9)$$

Non-trivial solutions of this system correspond to symmetric (+) (respectively antisymmetric (-)) modes with angular frequency $\omega_{p,+}$ (resp. $\omega_{p,-}$) and damping (full width at half maximum) γ_+ (resp. γ_-) given by

$$\omega_{p,\pm} = \text{Re}(\tilde{\omega}_{p,\pm}) = -\frac{c}{2l} (\arg[(r \pm t)r'] + 2p\pi) \quad (10)$$

$$\gamma_{\pm} = -2\text{Im}(\tilde{\omega}_{p,\pm}) = -\frac{c}{l} \log(|r \pm t||r'|) \quad (11)$$

where p is an integer corresponding to the longitudinal mode number. From Eq. (10), the frequency splitting

between symmetric and antisymmetric modes of identical longitudinal numbers is given by:

$$\Delta\nu = \frac{\omega_{p,+} - \omega_{p,-}}{2\pi} = \frac{c}{4\pi l} \arg\left(\frac{r-t}{r+t}\right) \quad (12)$$

Finally, if the membrane losses L_{\pm} and mirror losses $L' = 1 - |r'|^2$ are small, Eq. (11) simplifies to

$$\gamma_{\pm} \approx \frac{c}{2l} (L_{\pm} + L').$$

Hence, the damping of the symmetric and antisymmetric modes gives direct access to the two parameters L_+ and L_- .

To perform this measurement, a 32-mm long cavity is formed by two mirrors with transmission-limited losses $L' = 455$ ppm, and radii of curvature 20 mm. The PhC is set in the centre of the cavity, on a three-axis translation stage. In order to align the cavity axis with respect to the PhC, the end mirror is also mounted on a two-axis translation stage. Finally, the PhC frame is glued on a piezoelectric stack to allow for automatic scans of its z position over several free spectral ranges.

RESULTS AND DISCUSSION

A. Band diagram of the PhC

The physics of high contrast gratings has previously been described in detail [25, 26]. Here, we extend it to the case of a PhC, following from earlier work [16, 27]. The high-reflection properties of the PhC result from Fano resonances arising from an interference between the direct reflection from the PhC and light leaking out from internal high-Q guided modes in the PhC. To unveil the band structure of the guided modes, we calculate the transmission of the PhC by means of the Rigorous Coupled Wave Analysis (RCWA) [28] which is well suited to periodic structures such as our square lattice of holes (lattice parameter $\Lambda = 830$ nm, membrane thickness $h = 213$ nm, hole radius $r_h = 276$ nm). We begin the analysis with the unpatterned membrane limit for which the dielectric constant of both the membrane material and the holes is set to an average value $\epsilon_{\text{eff}} = \eta\epsilon_{\text{air}} + (1 - \eta)\epsilon_{\text{Si}_3\text{N}_4} = 2.95$. The field solutions are guided modes, referred to as ‘‘unperturbed modes’’ in the following discussion. They are plane waves reflected by total internal reflection upon the two faces of the membrane. In this regime, the unperturbed modes are evanescent outside of the membrane: the z component of their wavevector fulfils $k_{z,m} \in \mathbb{R}^+$ inside the membrane, and $k_{z,\text{air}} \in i\mathbb{R}^-$ in the surrounding medium. TE (TM) modes have their electric (magnetic) field within the plane of the membrane, and are represented on Fig. 3 in red (blue) respectively. The eight modes are sorted

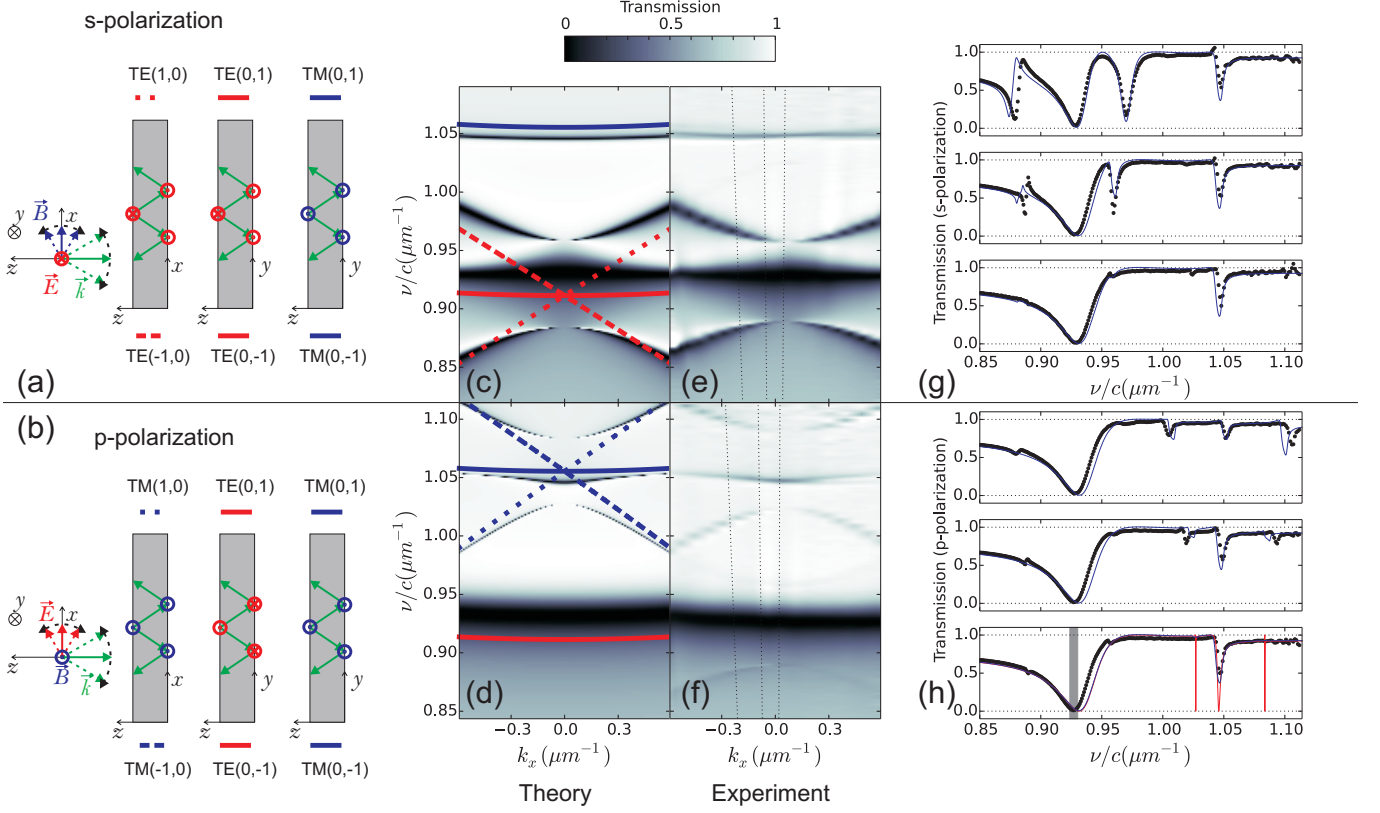


FIG. 3. (a),(b) First-order guided modes of an unpatterned membrane illuminated under s-polarization and p-polarization respectively. (c), (d) Theoretical reflectivity map of a 213 nm thick PhC patterned with a square lattice of period $\Lambda = 830$ nm, round hole filling factor $\eta = 30.6\%$, and dielectric constant given by [24], as a function of lateral wave-vector k_x , and normalized laser frequency ν/c under s-illumination (c), and p-illumination (d). The guided-resonance frequencies of the unpatterned membrane are superimposed, with TE-modes in red and TM-modes in blue (see (a) and (b) for the list of symbols). (e), (f) Experimental map of the reflectivity measured under s-illumination (e) and p-illumination (f). (g), (h) Experimental transmission (points) measured for an angle 3.57° , 1.23° and 0.33° (from top to bottom) for s-illumination (g) and p-illumination (h). The dashed lines of constant $k_x/k_{z,\text{air}}$ in (e) and (f) correspond to these measurements. The corresponding theoretical RCWA fit convoluted with the spectrometer response is plotted as a blue line. As an example, the unconvoluted RCWA result is plotted in red in the last cut of (h). In this plot, the shaded area corresponds to the wavelength range scanned in Fig. 4.

according to their symmetry class with respect to the xOz plane. Symmetric modes ($TM(\pm 1, 0)$) are not excited under s-illumination whereas antisymmetric modes ($TE(\pm 1, 0)$) are not excited under p-illumination. The complex coefficients describing the reflection inside the membrane for the electric field are given by Fresnel's law

$$r_{\text{TM}} = \frac{k_{z,m} - \epsilon_{\text{eff}} k_{z,\text{air}}}{k_{z,m} + \epsilon_{\text{eff}} k_{z,\text{air}}}, \quad r_{\text{TE}} = \frac{k_{z,\text{air}} - k_{z,m}}{k_{z,m} + k_{z,\text{air}}}.$$

We have numerically solved the round-trip resonance condition within the membrane

$$r_j^2 e^{-2ik_{z,m}h} = 1, \quad (13)$$

for $j = TE$ or TM , and for the lowest possible value of $\omega = c\sqrt{(k_x + 2p_x\pi/\Lambda)^2 + (2p_y\pi/\Lambda)^2 + k_{z,m}^2}$, (where $(p_x, p_y) = (\pm 1, 0)$ or $(0, \pm 1)$ are the diffraction orders in the x and y directions respectively). Note that the periodicity Λ is not a property of the unpatterned membrane

and that it is arbitrarily chosen to match that of the patterned membrane. Given the phases of r_{TE} and r_{TM} , we find that TE modes have a lower fundamental resonance frequency than TM modes. Finally, the symmetry of the mode with respect to the xOy plane is given by the sign of the half round-trip propagation coefficient

$$r_j e^{-ik_{z,m}h} = \pm 1. \quad (14)$$

From the expressions of r_{TE} and r_{TM} , it follows that the fundamental TE (resp. TM) mode is antisymmetric (symmetric) with respect to xOy . The calculated mode frequencies as a function of transverse wavevector k_x are represented by the lines in Fig. 3c and d. To first order, the frequency of the modes diffracted along the y direction is not affected by the transverse k_x component, contrary to the modes diffracted along the x direction.

The results of the RCWA for the patterned membrane are superimposed as a color plot in Fig. 3c and d (refrac-

tive index of Si_3N_4 given by [24]). In this case, the modes described in the unpatterned case are now coupled together by diffraction, giving rise to avoided crossings. In addition, the reflections at the membrane/air interfaces couple the guided modes to the zeroth-order modes propagating in free-space, leading to an effective loss channel. The guided resonances acquire a finite lifetime inversely proportional to the width of the Fano resonance (cut along a fixed value of k_x in Fig. 3). We find that the lifetime of TM modes is approximately 20 times that of TE modes. Note that at normal incidence the yOz plane constitutes an additional plane of (anti)-symmetry in the s- (p-) polarization, and hence, only the combinations $TE(1,0) + TE(-1,0)$ and $TM(0,1) + TM(0,-1)$ (resp. $TE(0,1) + TE(0,-1)$ and $TM(1,0) + TM(-1,0)$) are effectively coupled to free space modes: the linewidth of the other Fano resonances vanish close to $k_x = 0$. The white light angle-resolved spectrometer described previously allowed us to measure the band structure of guided modes for small transverse wave-vectors k_x . The experimental transmissions with s- (p-) illumination is presented in Fig. 3e and 3f, together with 3 different cuts with incidence angle 3.57° , 1.23° and 0.33° . The simulation is fitted to the data with the hole radius and membrane thickness as free parameters. Indeed, the former is only specified to within 10 % accuracy and the latter may differ from the design value due to imperfect pattern transfer upon electron-beam lithography and etching. The fitted values $r_h = 276$ nm and $h = 213$ nm are in good agreement with the design values. The theoretical fits are represented in blue in Fig. 3g and h. The reduced visibility of the peaks, particularly pronounced with TM modes, is well accounted for by convolving the theoretical map with the 4-nm wide response of the spectrometer. In the next section, we analyse in more detail the TE Fano resonance responsible for the largest dip in transmission close to $\nu = c \times 0.929 \mu\text{m}^{-1} = c/(1.076 \mu\text{m})$ in Fig. 3g and h.

B. Detailed characterization of a Fano resonance

For optical frequencies $\nu = c/\lambda$ close to a guided mode resonance, the PhC complex reflection and transmission coefficients r and t are given in good approximation by the simple two-mode model [27]

$$r(\lambda) = r_d \pm \frac{\gamma}{i(\lambda - \lambda_0) + \gamma} (\pm r_d - t_d) \quad (15)$$

$$t(\lambda) = t_d + \frac{\gamma}{i(\lambda - \lambda_0) + \gamma} (\pm r_d - t_d), \quad (16)$$

where r_d and t_d are the off-resonant coefficients ($|r_d + t_d| = |r_d - t_d| = 1$), λ_0 is the wavelength of the guided mode resonance, γ the resonance width, and the plus/minus sign in Eq. (15) reflects the symmetry

of the guided mode: as discussed in the previous section, the lowest order TE-mode is antisymmetric with respect to the xOy plane, and thus the minus sign applies. In the absence of optical losses, a striking feature of this Fano lineshape is the existence of a frequency $\lambda_1 = \lambda_0 + i\gamma r_d/t_d$ for which the PhC transmission vanishes: $T(\lambda_1) = |t(\lambda_1)|^2 = 0$, and accordingly, the reflectivity tends to unity: $R(\lambda_1) = |r(\lambda_1)|^2 = 1$.

By fitting the RCWA results with Eqs. 15 and 16 around the largest TE Fano resonance, we determine $\lambda_1 = 1076$ nm and $\gamma = 12$ nm. In order to study the optical behaviour of the PhC around λ_1 , a single-ended optical cavity of length l_0 was realized, using the PhC as end-mirror (see Fig. 2). The transmission of the cavity is monitored while a tunable diode laser is swept across the Fano resonance. The recorded signal, shown in Fig. 4a, displays a comb of peaks spaced by the free spectral range of the cavity given by

$$\Delta\lambda_{\text{FSR}} = \frac{\lambda_0^2}{2l_0}. \quad (17)$$

The three missing peaks at 1078.4, 1080.5, and 1080.8 nm correspond to mode hops of the laser. The linewidth $\Delta\lambda_n(\lambda)$ of each longitudinal cavity mode n is then obtained by fitting a Lorentzian profile to each of the individual peaks. To minimize the impact of scan speed fluctuations, we generate 50-MHz sidebands in the laser spectrum with an electro-optic modulator, used as a frequency calibration of the instantaneous scanning speed. Denoting the finesse of the cavity by $\mathcal{F}(\lambda)$, the total round-trip loss of the cavity is given by $\Gamma_{\text{RTL}}(\lambda) = 2\pi/\mathcal{F}(\lambda) = 2\pi\Delta\lambda_n(\lambda)/\Delta\lambda_{\text{FSR}}(\lambda)$. They are plotted in blue in Fig. 4b as a function of the laser wavelength. The lowest level of $\Gamma_{\text{RTL}} = (2130 \pm 150)$ ppm, corresponding to a finesse $\mathcal{F}(\lambda_1) = 2950 \pm 200$, or equivalently, a reflectivity $R(\lambda_1) = (99.79 \pm 0.02)\%$ was found at $\lambda_1 = 1079.1$ nm. The 3.1 nm discrepancy with respect to the results of Fig. 3 is quite small considering that two different membranes from the same micro-fabrication run were used in these experiments. In the simulations, it is accounted for by changing the hole radius from $r_h = 276$ nm to $r_h = 272$ nm.

To discriminate between the contributions of the membrane transmission $T(\lambda) = |t(\lambda)|^2$ and the optical losses $L(\lambda) = 1 - R(\lambda) - T(\lambda)$ in $\Gamma_{\text{RTL}}(\lambda)$, we use the extra-information embedded in the height of the transmitted peaks. Indeed, the transmission $\mathcal{T}_n(\lambda)$ of the cavity at resonance with the n^{th} mode is given by

$$\mathcal{T}_n(\lambda) = \frac{4T_c T(\lambda)}{\Gamma_{\text{RTL}}(\lambda)^2}, \quad (18)$$

where T_c is the transmission of the input mirror, assumed to be constant over the wavelength range scanned here. In the experiment, a signal proportional to $\mathcal{T}_n(\lambda)$ is measured, so that we can deduce $T(\lambda)$ from Eq. (18)

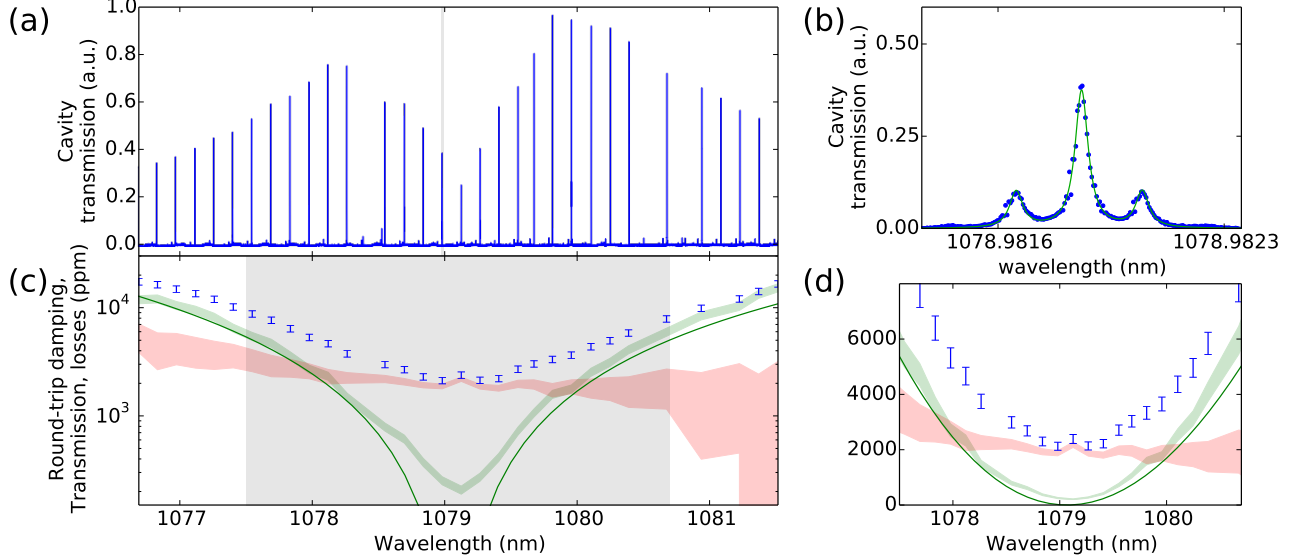


FIG. 4. (a) Transmission of a single-ended cavity as a function of laser wavelength. (b) Zoom of an individual Airy peak, showing modulation sidebands, and a Lorentzian fit. (c) Round-trip loss inferred from the fits of individual Airy peaks in blue. The error bars are extracted from the average off-centering of the central peak between left and right sidebands. The red and green shaded area represents the confidence interval for the PhC loss and transmission respectively. The green line is the theoretical transmission calculated by RCWA with the same parameters as Fig. 3, except for $r_h = 272$ nm (this experiment uses a second membrane from the same micro-fabrication run). (d) provides a linear representation of the data in (c).

within a multiplicative constant α . By assuming that the losses $L(\lambda)$ are within the interval $[0, \Gamma_{\text{RTL}}(\lambda_1)]$ at the highest accessible wavelength, we obtain a confidence interval for α , and hence for $T(\lambda) = \Gamma_{\text{RTL}}(\lambda) - L(\lambda)$ (in green on Fig. 4c and d) and for $L(\lambda)$ (in red) over the whole wavelength range. For comparison, the transmission calculated by RCWA is displayed with a green solid line on Fig. 4c and d. The agreement between RCWA and experimental results is excellent. At the Fano resonance $\lambda_1 = 1079.1$ nm, the round-trip damping is vastly dominated by membrane losses. The lowest cavity bandwidth $\kappa/2 = c/4l\mathcal{F}(\lambda_1) = 6.2$ MHz measured in this single-ended cavity setup approaches the resolved-sideband condition for first-order flexure modes of the suspended membrane.

To understand the exact form of the scattering matrix, and gain insight on the origin of the losses observed in the previous experiment, a PhC is positioned in the middle of a high-finesse cavity. The PhC position Δl is scanned along the cavity axis with a piezoelectric actuator. In this configuration, the PhC couples two cavities of length $l_1 + \Delta l/2$, and $l_2 - \Delta l/2$, where $l_1 \approx l_2 \approx l$ are the initial lengths of the first and second sub-cavities, supposed to be simultaneously resonant with the central laser wavelength λ_c for $\Delta l = 0$. The cavity transmission, recorded as a function of Δl and laser detuning $\delta\nu \propto \lambda_c - \lambda$, is represented in the color plots of Fig. 5a, b and c. The avoided crossing of symmetric and antisym-

metric modes is visible in the centre of the figure. From a Lorentzian fit of the peaks at the avoided crossing and along the vertical axis, we extract the frequency spacing $\Delta\nu$, and the linewidth γ_{\pm} of symmetric and antisymmetric modes. The experiment is then reproduced for several laser wavelengths λ_c close to the Fano resonance and the corresponding frequency spacings and linewidths are shown in Fig. 5d and e respectively.

In Fig. 5a and c, the upper and lower branches of the avoided crossing are strongly asymmetric. This is a direct consequence of the difference between L_+ and L_- . For $\lambda_c < \lambda_1$ (Fig. 5a), the phase of $(r - t)/(r + t)$ is positive, such that from Eq. (12), the symmetric mode (angular frequency ω_+) constitutes the upper branch of the crossing, while the antisymmetric mode (angular frequency ω_-) is the lower branch. On the other hand, for $\lambda_c > \lambda_1$ (Fig. 5c), $\Delta\nu = (\omega_+ - \omega_-)/2\pi$ changes its sign and the upper and lower branches are exchanged. Finally, at the Fano resonance $\lambda_c = \lambda_1$, r and t are in phase, so that symmetric and antisymmetric modes are perfectly degenerate. Combined with the inequalities of Eq. (3), an upper bound for the transmission of the membrane can be derived: $|t| \leq 1 - |r|$ at the Fano resonance. For $1 - R = 2130$ ppm, this corresponds to a transmission as low as $T \leq 1.1$ ppm. Hence, the residual transmission of 210 ppm observed in Fig. 4 is somehow in contradiction with the two-port description developed in this work. A first explanation is the possible scattering into

non-overlapping spatial modes due to surface roughness. Moreover, given our experimental parameters, we expect from RCWA that the wavevector components of the input Gaussian beam not aligned with a symmetry plane of the membrane should give rise to ≈ 20 ppm transmission into the polarization orthogonal to the input beam (with a spatial wavefunction that is antisymmetric with respect to the xOz and yOz planes). Nevertheless, as visible on Fig. 4, the residual transmission only accounts for a small fraction of the total cavity losses close to the Fano-resonance, and the nature of these losses still needs to be elucidated.

The difference between the losses L_{\pm} experienced by the symmetric and antisymmetric modes is well captured by a simple phenomenological model: since the Fano resonance results from the interference between the direct PhC transmission and a high-Q guided resonance, it can be safely assumed that the losses mostly affect the former. Hence, Eqs. (15) and (16) are modified to include a phenomenological loss rate γ' to the high-Q response as

$$r = r_d - \frac{\gamma}{i(\lambda - \lambda_0) + \gamma + \gamma'}(-r_d - t_d)$$

$$t = t_d + \frac{\gamma}{i(\lambda - \lambda_0) + \gamma + \gamma'}(-r_d - t_d).$$

Using this model, it follows that

$$L_+ = 0 \quad (19)$$

$$L_- = \frac{4\gamma\gamma'}{(\gamma + \gamma')^2 + (\lambda - \lambda_0)^2}, \quad (20)$$

and thus, only the antisymmetric mode of the two-cavity setup is affected by the optical losses, with a value proportional to the Lorentzian response of the guided resonance. This is an intuitive result since the antisymmetric guided resonance under study isn't driven by a symmetric incoming field (this would be vice-versa for the symmetric TM resonance). To quantitatively evaluate the model, Fig. 5e shows the total expected linewidths $L_{\pm} + L'$, where $\gamma' = 1.0 \times 10^{-2}$ nm is the only adjustable parameter, since $\lambda_1 = 1079.1$ nm, $\gamma = 12$ nm and $L' = 455$ ppm are independently determined. Therefore, optical losses are found to account for less than 0.1 % in the total decay rate of the guided mode resonance. The previous model shows that the asymmetry between L_+ and L_- is a direct consequence of the physics of Fano-resonances, and contrary to a theoretical modelling recently proposed [29], this shows that it is not specific to a particular loss mechanism such as absorption or scattering, since both would preferentially affect the high-Q guided mode. However, if the losses observed in this experiment were entirely due to optical absorption, the value $\text{Im}(n) = (3.5 \pm 1.5) \times 10^{-5}$ could be derived for the absorption of the Si_3N_4 layer. The values of $L_{\pm} + L'$ obtained with a RCWA simulation including an absorption $2 \times 10^{-5} \leq \text{Im}(n) \leq 5 \times 10^{-5}$ are located within the

shaded areas in Fig. 5e. Since previous experiments [30] have found values for the absorption of a similar layer an order of magnitude smaller ($\text{Im}(n) = 2.0 \times 10^{-6}$), we conclude that scattering is still the main source of losses. In the single-ended cavity case where the field is essentially incident on one side of the membrane, the relevant optical losses are given by $L = (L_+ + L_-)/2$. Thus, the decrease of optical losses with optical wavelength visible in Fig. 4b is consistent with Eq. 19 and 20. With the previous smaller value of Si_3N_4 absorption, a RCWA simulation shows that a reflectivity as high as $R \approx 1 - 80$ ppm, corresponding to a finesse close to 80 000, could be achieved by improving the PhC fabrication process.

CONCLUSIONS

High-stress Si_3N_4 films have been successfully patterned to realize a 2D photonic crystal. We have provided a detailed study of the rich mode structure underlying the high-reflectivity of the crystal. We have fully characterized the scattering and loss properties of the device. We have experimentally demonstrated the wide tunability of the membrane reflectivity, via the adjustment of the laser wavelength close to a Fano resonance. Such tunability is highly desirable in the context of membrane-in-the-middle optomechanics experiments. In particular, the ability to reach very narrow energy gap between the eigenmodes of the coupled cavities could be used to enter the regime where the photon exchange time becomes comparable to the mechanical motion period. This would enable the observation of mechanically-induced coherent photon dynamics, like Autler-Townes splitting or Landau-Zener-Stueckelberg dynamics [20], thus bringing tools that are commonly used in atomic physics to the field of optomechanics. Finally, the bandwidth of the single-ended cavity described in this work is close from the requirement to place a drum mode of the membrane in the resolved sideband regime and we have been able to reduce it to 2.4 MHz by increasing the cavity length. Hence, this technique is already suitable for the development of optomechanical transducers.

ACKNOWLEDGEMENTS

The authors gratefully acknowledge M. Corcos, I. Krasnokutskaya, X. Pennehouat and L. Pinol for preliminary experimental developments. We thank J. Palomo and M. Rosticher for developing the first steps of the microfabrication process. Finally, we thank J. Lawall and R. Gu erout for insightful scientific discussions. This research has been partially funded by the Agence Nationale de la Recherche programs ‘‘ANR-2011-BS04-029 MiNO-ToRe’’ and ‘‘ANR-14-CE26-0002 QuNaT’’, the Marie Curie Initial Training Network ‘‘cQOM’’, and the DIM

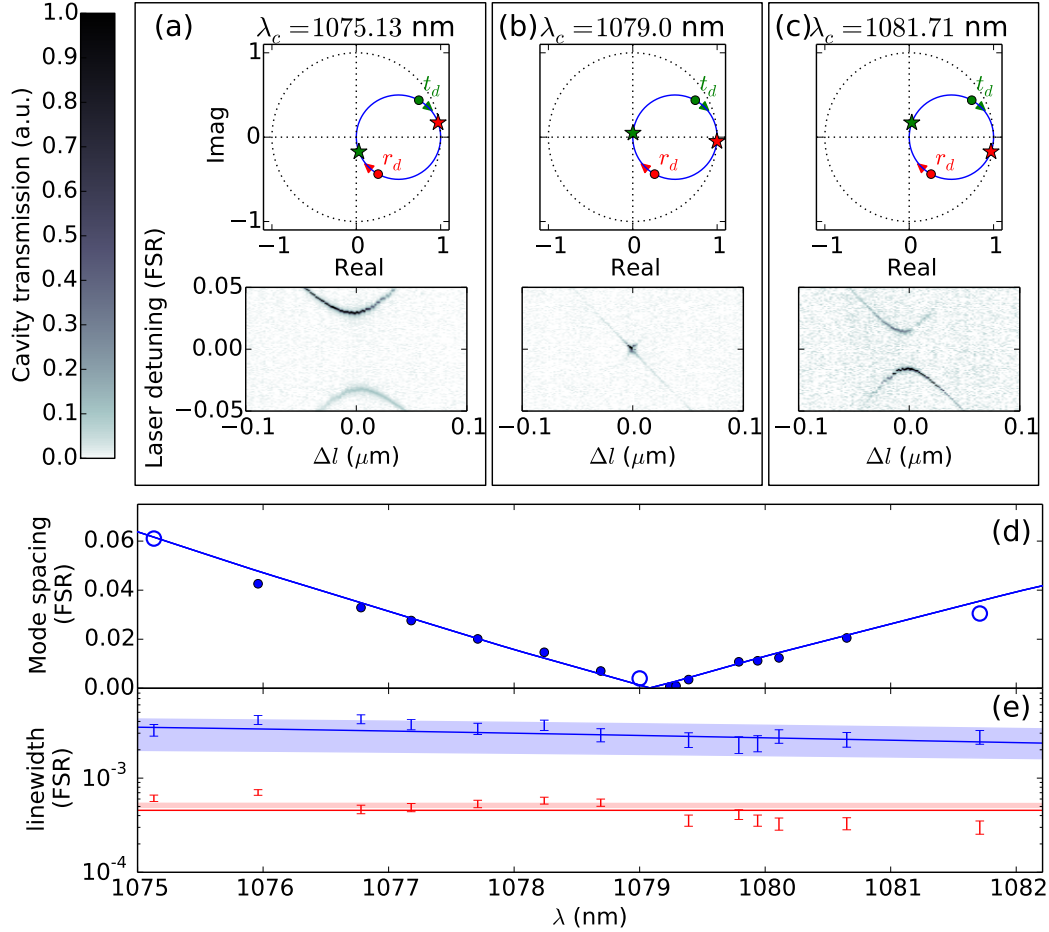


FIG. 5. (a), (b) and (c) show colorplots of the cavity transmission versus the cavity length and laser detuning with respect to three different laser central wavelengths λ_c . Above are the corresponding complex representations of $r(\lambda)$ and $t(\lambda)$, where a global phase factor has been applied to ensure that $r(\lambda_1) = r_d + t_d = 1$. The green and red bullets correspond to $r(\lambda_0) = t_d$ and $t(\lambda_0) = r_d$ respectively, the green and red stars correspond to $t(\lambda_c)$ and $r(\lambda_c)$ respectively. In (a) ((c)), λ_c is chosen smaller (larger) than λ_1 . In (b), λ_c is chosen very close to λ_1 , so that $r(\lambda_c) \simeq 1$ and $t(\lambda_c) \simeq 0$. (d) Mode frequency spacing for $\Delta l = 0$. A minimum is reached for $\lambda = \lambda_1$. The blue line corresponds to the mode spacing calculated by RCWA using Eq. (12) (same parameters as in Fig. 4). (e) Linewidths of the two modes. The blue strip represents the value obtained with RCWA simulations including an absorption of $2 \times 10^{-5} \leq \text{Im}(n) \leq 5 \times 10^{-5}$. Optical detunings are normalized by the FSR of the sub-cavities $\Delta\lambda_{\text{FSR}} = \lambda_c^2/2l$. The error bars are inferred from the variation of the fit parameters obtained with neighbouring values of Δl .

nano-K Ile-de-France program “NanoMecAtom”. S. C. is supported by the Marie Skłodowska-Curie Individual Fellowship program.

* Current affiliation: IBM Research - Zürich, Säumerstrasse 4, 8803 Rüschlikon, Switzerland

[1] Teufel JD, Donner T, Li D, Harlow JW, Allman MS, Cicak K, et al. Sideband cooling of micromechanical motion to the quantum ground state. *Nature*. 2011;475:359–363. Available from: <http://dx.doi.org/10.1038/nature10261>.

[2] O’Connell AD, Hofheinz M, Ansmann M, Bialczak RC, Lenander M, Lucero E, et al. Quantum ground state and single-phonon control of a mechanical resonator. *Nature*. 2010;464:697–703. Available from: <http://dx.doi.org/10.1038/nature08967>.

[3] Safavi-Naeini AH, Chan J, Hill JT, Alegre TPM, Krause A, Painter O. Observation of Quantum Motion of a Nanomechanical Resonator. *Physical Review Letters*. 2012;108:033602. Available from: <http://link.aps.org/doi/10.1103/PhysRevLett.108.033602>.

[4] Purdy TP, Peterson RW, Regal CA. Observation of Radiation Pressure Shot Noise on a Macroscopic Ob-

- ject. *Science*. 2013 sep;339:801. Available from: <http://arxiv.org/abs/1209.6334>.
- [5] Romero-Isart O, Pflanzner AC, Blaser F, Kaltenbaek R, Kiesel N, Aspelmeyer M, et al. Large quantum superpositions and interference of massive nanometer-sized objects. *Physical Review Letters*. 2011;107:1–4.
- [6] Pirkkalainen JM, Cho SU, Li J, Paraoanu GS, Hakonen PJ, Sillanpää Ma. Hybrid circuit cavity quantum electrodynamics with a micromechanical resonator. *Nature*. 2013;494:211–5. Available from: <http://www.ncbi.nlm.nih.gov/pubmed/23407536>.
- [7] Yeo I, de Assis PL, Gloppe A, Dupont-Ferrier E, Verlot P, Malik NS, et al. Strain-mediated coupling in a quantum dot-mechanical oscillator hybrid system. *Nature Nanotechnology*. 2014;9:106–10. Available from: <http://www.ncbi.nlm.nih.gov/pubmed/24362234>.
- [8] Rabl P, Kolkowitz SJ, Koppens FHL, Harris JGE, Zoller P, Lukin MD. A quantum spin transducer based on nanoelectromechanical resonator arrays. *Nature Physics*. 2010 may;6:602–608. Available from: <http://www.nature.com/doi/10.1038/nphys1679>.
- [9] Kolkowitz S, Jayich ACB, Unterreithmeier QP, Bennett SD, Rabl P, Harris JGE, et al. Coherent sensing of a mechanical resonator with a single-spin qubit. *Science (New York, NY)*. 2012 mar;335:1603–6. Available from: <http://science.sciencemag.org/content/335/6076/1603.abstract>.
- [10] Jöckel A, Faber A, Kampschulte T, Korppi M, Rakher MT, Treutlein P. Sympathetic cooling of a membrane oscillator in a hybrid mechanical-atomic system. *Nature nanotechnology*. 2014;10:11. Available from: <http://arxiv.org/abs/1407.6820>.
- [11] Andrews RW, Peterson RW, Purdy TP, Cicak K, Simmonds RW, Regal CA, et al. Bidirectional and efficient conversion between microwave and optical light. *Nature Physics*. 2014;10:321–326. Available from: <http://dx.doi.org/10.1038/nphys2911>.
- [12] Bağcı T, Simonsen A, Schmid S, Villanueva LG, Zeuthen E, Appel J, et al. Optical detection of radio waves through a nanomechanical transducer. *Nature*. 2014;507:81–5. Available from: <http://www.ncbi.nlm.nih.gov/pubmed/24598636>.
- [13] Purdy TP, Peterson RW, Yu PL, Regal CA. Cavity optomechanics with Si₃N₄ membranes at cryogenic temperatures. *New Journal of Physics*. 2012 nov;14:115021. Available from: <http://stacks.iop.org/1367-2630/14/i=11/a=115021?key=crossref.11356b3176442bddf1dcc4ae5ae5b3b0>.
- [14] Regal CA, Lehnert KW. From cavity electromechanics to cavity optomechanics. *Journal of Physics: Conference Series*. 2011 jan;264:012025. Available from: <http://stacks.iop.org/1742-6596/264/i=1/a=012025?key=crossref.9a33e0272f3a3a1ddcc65e145da6674d>.
- [15] Unterreithmeier QP, Weig EM, Kotthaus JP. Universal transduction scheme for nanomechanical systems based on dielectric forces. *Nature*. 2009;458:1001–4. Available from: <http://dx.doi.org/10.1038/nature07932>.
- [16] Makles K, Antoni T, Kuhn AG, Deléglise S, Briant T, Cohadon PF, et al. 2D photonic-crystal optomechanical nanoresonator. *Opt Lett*. 2015;40:174–177. Available from: <http://ol.osa.org/abstract.cfm?URI=ol-40-2-174>.
- [17] Schliesser A, Riviere R, Anetsberger G, Arcizet O, Kippenberg TJ. Resolved-sideband cooling of a micromechanical oscillator. *Nat Phys*. 2008 may;4(5):415–419. Available from: <http://dx.doi.org/10.1038/nphys939>http://www.nature.com/nphys/journal/v4/n5/supinfo/nphys939/_S1.html.
- [18] Thompson JD, Zwickl BM, Jayich aM, Marquardt F, Girvin SM, Harris JGE. Strong dispersive coupling of a high-finesse cavity to a micromechanical membrane. *Nature*. 2008 mar;452:72–5. Available from: <http://www.ncbi.nlm.nih.gov/pubmed/18322530>.
- [19] Kemiktarak U, Metcalfe M, Durand M, Lawall J. Mechanically compliant grating reflectors for optomechanics. *Applied Physics Letters*. 2012;100:061124. Available from: <http://scitation.aip.org/content/aip/journal/apl/100/6/10.1063/1.3684248>.
- [20] Heinrich G, Harris JGE, Marquardt F. Photon shuttle: Landau-Zener-Stückelberg dynamics in an optomechanical system. *Physical Review A*. 2010 jan;81:011801. Available from: <http://link.aps.org/doi/10.1103/PhysRevA.81.011801>.
- [21] Norcada;. www.norcada.com.
- [22] Yuan M, Cohen MA, Steele GA. Silicon nitride membrane resonators at millikelvin temperatures with quality factors exceeding 108. *Applied Physics Letters*. 2015;107(26). Available from: <http://scitation.aip.org/content/aip/journal/apl/107/26/10.1063/1.4938747>.
- [23] Arduino;. www.arduino.cc/.
- [24] Dielectric permittivity of Si₃N₄; $\epsilon_{\text{Si}_3\text{N}_4} = 1 + 2.8939\lambda^2/(\lambda^2 - (0.13867\mu\text{m})^2)$. (from Ref. [31]).
- [25] Karagodsky V, Sedgwick FG, Chang-Hasnain CJ. Theoretical analysis of subwavelength high contrast grating reflectors. *Optics express*. 2010;18:16973–16988.
- [26] Karagodsky V, Chang-Hasnain CJ. Physics of near-wavelength high contrast gratings. *Optics Express*. 2012;20:10888.
- [27] Fan S, Joannopoulos J. Analysis of guided resonances in photonic crystal slabs. *Physical Review B*. 2002;65(23):235112. Available from: <http://link.aps.org/doi/10.1103/PhysRevB.65.235112>.
- [28] Liu V, Fan S. S 4: A free electromagnetic solver for layered periodic structures. *Computer Physics Communications*. 2012;183:2233–2244. Available from: <http://dx.doi.org/10.1016/j.cpc.2012.04.026>.
- [29] Stambaugh C, Xu H, Kemiktarak U, Taylor J, Lawall J. From membrane-in-the-middle to mirror-in-the-middle with a high-reflectivity sub-wavelength grating. *Annalen der Physik*. 2014 oct;8:81–88. Available from: <http://doi.wiley.com/10.1002/andp.201400142>.
- [30] Serra E, Bawaj M, Borrielli A, Di Giuseppe G, Forte S, Kralj N, et al. Microfabrication of large area high-stress silicon nitride membranes for optomechanical devices. *arXiv*. 2015; Available from: <http://arxiv.org/abs/1601.02669>.
- [31] Philipp HR. Optical Properties of Silicon Nitride. *J Electrochem Soc*. 1973;120:295–300.